High-resolution model building with multistage full-waveform inversion for narrow-azimuth acquisition data

Jian Mao[1], James Sheng[1], Matt Hart[1], and Taejong Kim[1]

Abstract

Full-waveform inversion (FWI) is an attractive tool for high-resolution velocity-model building without a high-frequency assumption compared to conventional reflection tomography. However, there are two main challenges to the application of FWI on narrow-azimuth acquisition (NAZ) data: cycle skipping and acquisition footprints. Here, a multistage FWI is proposed to build a high-resolution model for NAZ data. It is well known that FWI may suffer from a cycle-skipping problem when the starting model is not close enough to the true solution. To mitigate this problem, we introduce dynamic-warping preconditioned full-waveform inversion (DWFWI) as the first stage of the velocity inversion. DWFWI iteratively preconditions the observed early arrivals through dynamic warping to avoid cycle skipping in the model, which allows large-scale background updates. The second stage of our workflow is the conventional FWI with image-guided smoothing (IGFWI). On top of DWFWI, more reflection events are included and inverted through the conventional L2-norm FWI, which can add more detailed updates to the velocity model with much higher resolution. Due to poor crossline sampling, there are strong acquisition footprints on FWI updates in the crossline direction. Image-guided smoothing is used to reduce the acquisition footprints in the FWI gradient as well as to preserve the detailed update around the faults. It is then followed by an additional tomography to update the deep portion. This approach was applied on the Hoop Fault Complex data in the southwestern Barents Sea. The results show that a more geologically realistic and higher-resolution model of the Hoop Fault Complex was obtained, and the migration image and gathers were significantly improved.

Introduction

High-resolution velocity-model building is critical for depth imaging to reduce artifacts or distortions in the migration image. A high-resolution tomographic inversion with offset-dependent residual-moveout picking and image-guided preconditioning (Hilburn et al., 2014) is developed to enforce the update to honor structures (layers and faults) automatically and provide a high-resolution update, which resolves fine features in the velocity model. However, its resolution is still restricted due to ray-tracing limitations. Full-waveform inversion (FWI) (Tarantola, 1984; Pratt et al., 1998; Sheng et al., 2006; Virieux and Operto, 2009; Warner et al., 2013) has been developed over the years to provide a higher-resolution velocity update, which is more geologically plausible with a built-in structure-oriented feature.

FWI seeks an optimized subsurface model by minimizing the differences between recorded and synthetic seismic data, which is a highly nonlinear optimization problem. When the time shifts between the synthetic and observed data are larger than one half cycle, the model is cycle skipped, and it can prevent convergence of FWI (Virieux and Operto, 2009; Warner et al., 2013). To mitigate the cycle-skipping problem, a previous reflection tomography model can be used as the FWI initial model with inversion starting from a low frequency and gradually increasing to a higher frequency; or, other objective functions can be adopted, which may be less affected by cycle skipping: adaptive waveform inversion (Warner and Guasch, 2015), Laplacian-Fourier domain FWI (Shin and Cha, 2009), reflection traveltime inversion with dynamic warping (Ma and Hale, 2013), full traveltime inversion (Luo et al. 2016), and envelope inversion (Wu et al., 2014). Here, we propose a method of dynamic warping preconditioned FWI (DWFWI) to precondition the observed data through dynamic warping such that the preconditioned data is within one half-period shift from the synthetic data. This DWFWI provides large-scale background updates without cycle skipping. After DWFWI, the conventional L2-norm FWI is performed to get a higher-resolution model update. As we know, FWI is a computationally demanding method, which requires a lot of resources for the 3D case. With an implementation on a graphics processing unit (GPU) for multiscale FWI (Mao et al., 2012), we have the ability to deal with large 3D data sets with a very quick turnaround time.

For NAZ acquisition, poor crossline sampling can cause strong acquisition footprints in the FWI update even after we applied preconditioning to the FWI gradient with diagonal Hessian. These footprints can be reduced by some regular smoothing operator. However, some detailed updates can be destroyed by regular smoothing. K_x-K_y domain filter (Jones et al., 2013) is effective, but it still cannot fully resolve and may generate some other artifacts without careful parameter selection. Here, we proposed to use image-guided smoothing to further reduce the footprint effects while we preserve the sharp contrast update around some key structures (e.g., faults).

This multistage FWI workflow (DWFWI + IGFWI) is applied to a 600 km^2 subset of a NAZ data set, the Hoop Fault Complex, which is 2770 km^2 acquired in 2009, located in the region of the Norwegian Barents Sea, and divides the Loppa High and Bjameland Platform. If the velocity profile is not modeled correctly across the fault boundary, distortions in the depth of the structure can be introduced. Large fault sags will show up within the footwall of the major trending extensional fault in the survey area, as well as numerous smaller distortions associated with complex faulting within the high-velocity Lower Cretaceous overburden. There are several prior studies to solve the fault shadow problem. Rodriguez et al. (2011) used fault-constrained tomography in this area, where velocity models were separated by an interpreted fault and updated independently. Hart et al. (2015) used offset-dependent picking and image-guided tomography (IGT) for a higher-resolution and more geologically consistent

[1]TGS.

http://dx.doi.org/10.1190/tle35121031.1.

approach to tomographic model building. Here we further improved the model resolution with FWI.

We use the IGT velocity model as the starting model for FWI. First, we apply DWFWI to match the major traveltime difference of the early arrivals and produce large-scale updates without cycle skipping. Then the conventional L2-norm FWI with image-guided smoothing is employed to produce a high-resolution update. Image-guided smoothing can reduce the footprint effect while preserving the sharp contrast around the faults. A much higher-resolution model results from this multistage FWI workflow. After FWI, we also applied an additional tomography to update the deep portion and avoid some overcorrected updates from FWI. Both the stacked image and common-image gathers (CIG) show the improvements from the advanced model-building approach.

Dynamic-warping preconditioned FWI

Dynamic warping (DW) (Hale, 2013) is proposed to estimate relative time shifts between observed and synthetic data. DW works much better than crosscorrelation-based methods when the shifts are large and vary rapidly with time and space and where seismic data is contaminated by noise. DW also can avoid the cycle-skipping problem and estimate traveltime shifts more accurately (Ma and Hale, 2013). Here, we precondition the observed data through dynamic warping for refraction FWI, because the similarity of early arrivals is usually very good between observed and synthetic data. The preconditioned data is the shifted synthetic data through DW. With limited maximum time shift in DW, the warped data is within one half-period time shift from the synthetic data for each shot during each iteration, which avoids cycle skipping. DWFWI also can mitigate the amplitude mismatch issue between real and modeled data. The reason for the mismatches is that the synthetic generation by the forward-modeling engine cannot fully simulate the real-world earth wave propagation. Through DW, there is only traveltime difference between synthetic data and warped data, which will be inverted without amplitude issue.

Figures 1a and 1b show the raw shot gather and the preprocessed data after low-pass filtering (up to 10 Hz), muting, and some minor denoising. Figure 1c is the synthetic data with the initial model using the estimated wavelet. We can see a traveltime difference between the observed data (Figure 1b) and the synthetic data with the initial model (Figure 1c) (the red lines are in the same position for each shot gather). After DW, we produce the warped synthetic data (Figure 1d), which shows the traveltime is matched with observed data. The warped synthetic will be the input for FWI, as there are no amplitude issues and it is free of noise. Figure 2 shows the starting model and velocity update with DWFWI (up to 10 Hz) for the Hoop Fault Complex data set, which is mainly a low-wavenumber background velocity update. After DWFWI, we have better matched the early-arrival refraction events when we compare the observed data and synthetic data. We also QC with depth-migrated common-image gathers (CIGs) shown in Figure 3. The gather flatness is improved a lot after DWFWI. The initial CIGs are not flat because the far-offset (large angle) part is muted for previous tomography. As we see, some noises and residual multiples also show up on the CIGs. We need to be careful on the picking because some picking on the multiple events will result in a wrong update for tomography. However, the DWFWI with refraction traveltime is very robust for the background update. This is the first stage our FWI workflow, which can solve the major traveltime differences and bring the velocity model close enough for conventional FWI.

FWI with image-guided smoothing

With DWFWI, we mitigate the cycle-skipping problem and get a more accurate velocity as the starting velocity. Then, we can turn on the conventional FWI to get further updates in a multiscale way, which means we run FWI to match the data from low

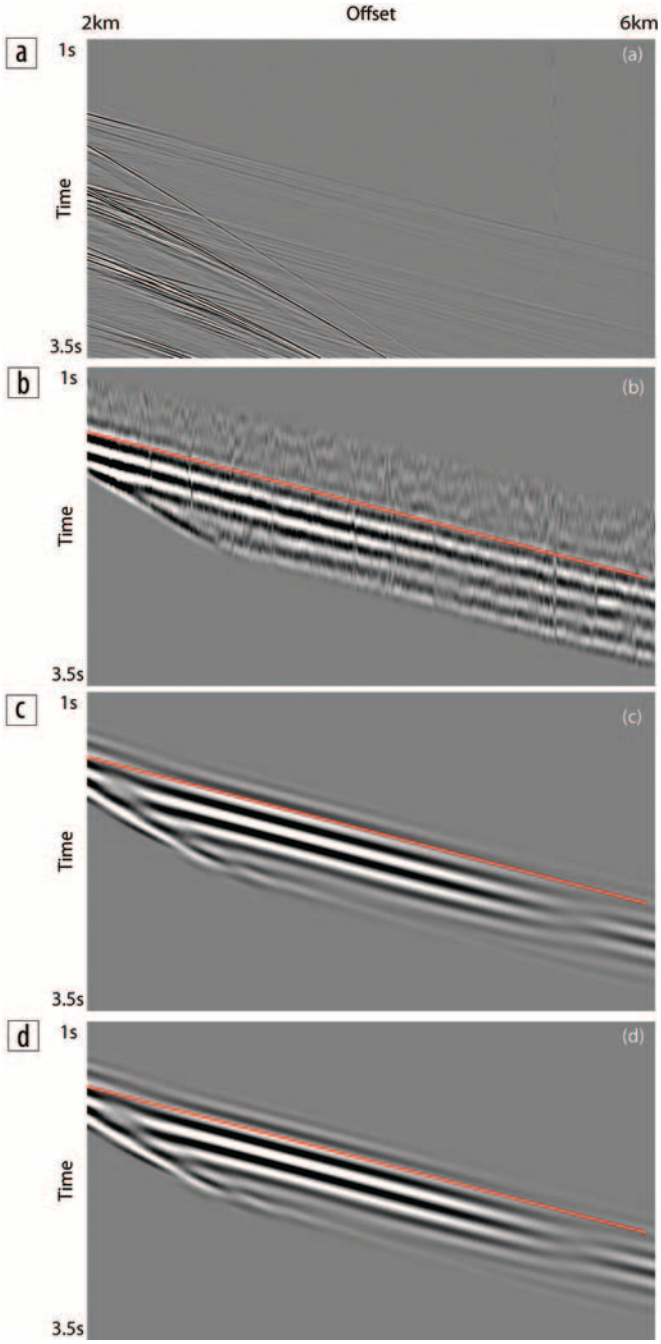

Figure 1. (a) Observed raw data. (b) Observed data after low-pass filtering and muting. (c) Synthetic data. (d) Warped synthetic data.

frequency to high frequency (up to 15 Hz). In this second stage, we can obtain a much higher-resolution update.

During the application of FWI on a NAZ data, we noticed a very strong acquisition footprint in the FWI update. First, we applied preconditioning to the FWI gradient with illumination (diagonal Hessian), which makes the update much more balanced, but the footprint effect still can be seen. Besides the footprint, we also notice migration swing artifacts on the FWI gradient due to insufficient coverage in the crossline direction. Therefore, we must apply smoothing to precondition the FWI gradient to avoid an inaccurate update. With a regular smoothing method, the resolution of the update is decreased a lot while reducing the footprint. This is why we adopted image-guided smoothing which is much more advanced than a regular smoothing method.

Image-guided smoothing is a kind of structure-oriented smoothing method. Ma et al. (2012) proposed image-guided FWI. They represent a model with a sparse set of values and use image-guided interpolation and its adjoint operator to compute finely and uniformly sampled models in FWI. Image-guided interpolation honors the imaged structures, so image-guided FWI can build a model which is more blocky and geologically sensible. With a migration image as reference, some control points are automatically selected on the image to generate the attribute used for smoothing. Then a nonuniform smoothing can be applied on the FWI gradient, which allows larger smoothing in areas with continuous events and less or no smoothing in areas with faults. Then the footprints and swing noise can be minimized with image-guided smoothing.

Figure 4 is the comparison of different preconditioning methods on FWI gradient. We can see a very strong footprint in the crossline direction due to the NAZ acquisition, which is shown in Figure 4a. With a regular smoothing method, we get a velocity update as Figure 4b shows. Figure 4c shows FWI with image-guided smoothing preconditioning, which is free of the footprint problem and the update is blocky. By comparing Figures 4b and 4c, we note as another important feature that the IGFWI preserved the sharp boundaries of the velocity update along the major faults. However, the regular

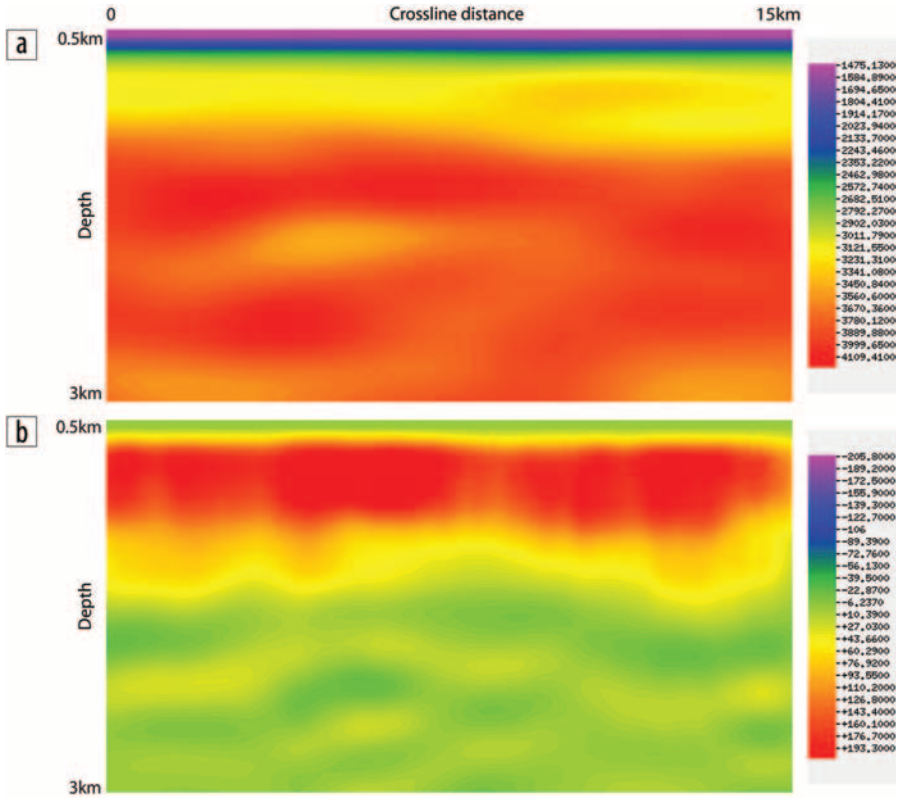

Figure 2. (a) Crossline section of the starting velocity. (b) Crossline section of the velocity update from DWFWI.

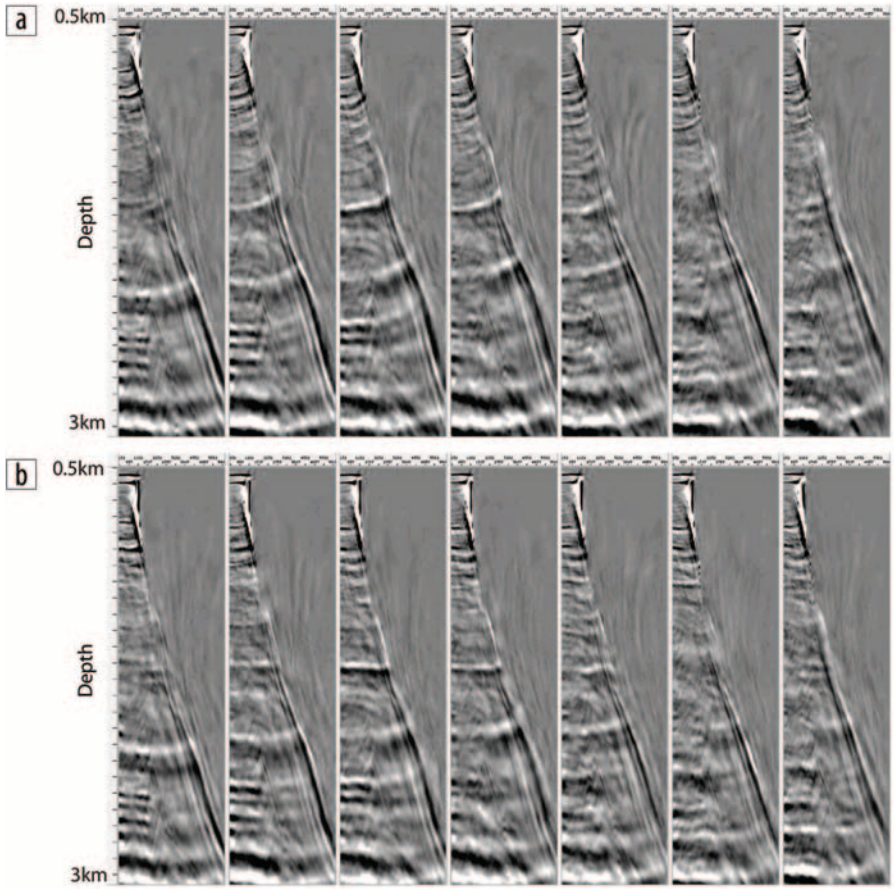

Figure 3. Common-image gathers (CIGs) of a crossline section. (a) CIG with the initial model. (b) CIG with the DWFWI model.

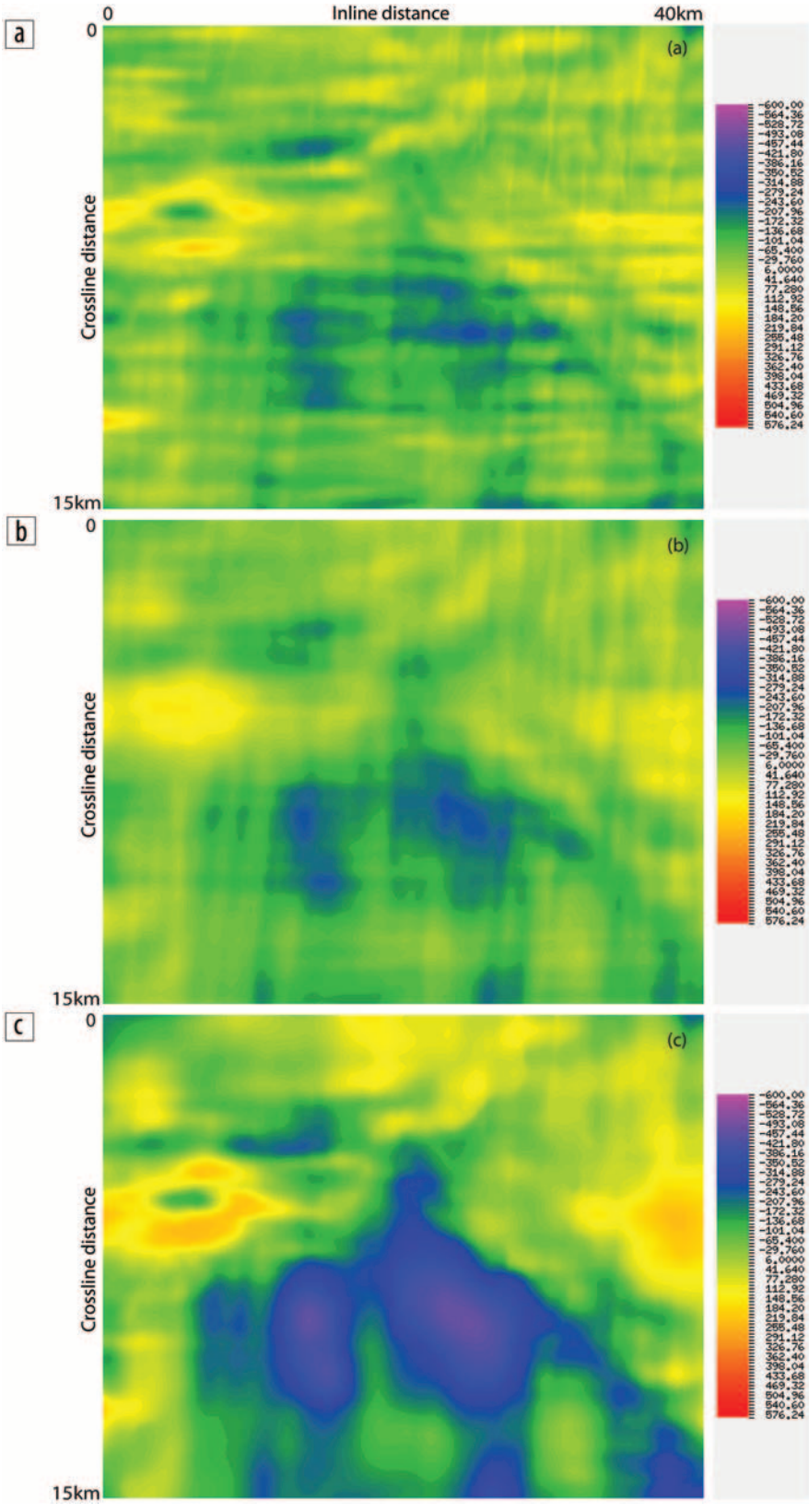

Figure 4. Comparison of FWI updates at depth 1050 m: (a) update without smoothing, (b) update with regular smoothing, and (c) update with IG smoothing.

smoothing method killed those details. All three FWI updates came from the same number of iterations, and we see better misfit drop from IGFWI, which provides larger amounts of updates. Since the footprint is knocked down and the sharp contrast is preserved in IGFWI gradient, it allows the update to go further than the other two, which provide better data match. If we migrate with the update from Figure 4a, there will be a lot of sags on the migration image in the crossline direction. With the update in Figure 4b, the image sags in the fault shadow area is not reduced much. IGFWI provided the best result for depth migration, which is shown in the next section.

Field data example with the Hoop Fault Complex

Our testing area in the Hoop Fault Complex is 15 km by 40 km. There are 43 sail lines in the data set for a total of more than 90,000 individual shots. Shot and receiver intervals are 18.75 m and 12.5 m. The streamer cable length is 6 km. The shot record length is 7.1 seconds. The sea bottom is nearly flat in the depth range of 0.43 km to 0.46 km. For the FWI test, the maximum frequency is up to 15 Hz. We applied some minor noise removal to the data set, but deghosting and demultiple were not applied. We begin with a Ricker wavelet for modeling and then get an updated source wavelet for inversion.

In FWI, we use the anisotropic VTI acoustic wave equation with a free-surface boundary condition. Anisotropic parameters ε and δ were fixed, and only the vertical velocity was updated. The diving-wave penetration is less than 3 km in depth. Each trace in the observed and the synthetic data has been normalized for the inversion. In the first stage, the input was muted with a combination of the water-bottom traveltime and a multipoint muting function, which mainly keeps the refraction energy in the input. We began the FWI with the transmitted early arrivals to update the lowest wavenumber velocity structure. In this stage, we used dynamic warping to match the major traveltime, which can reduce the cycle-skipping problem. After the major update is complete, additional iterations of conventional FWI were run sequentially with multifrequency

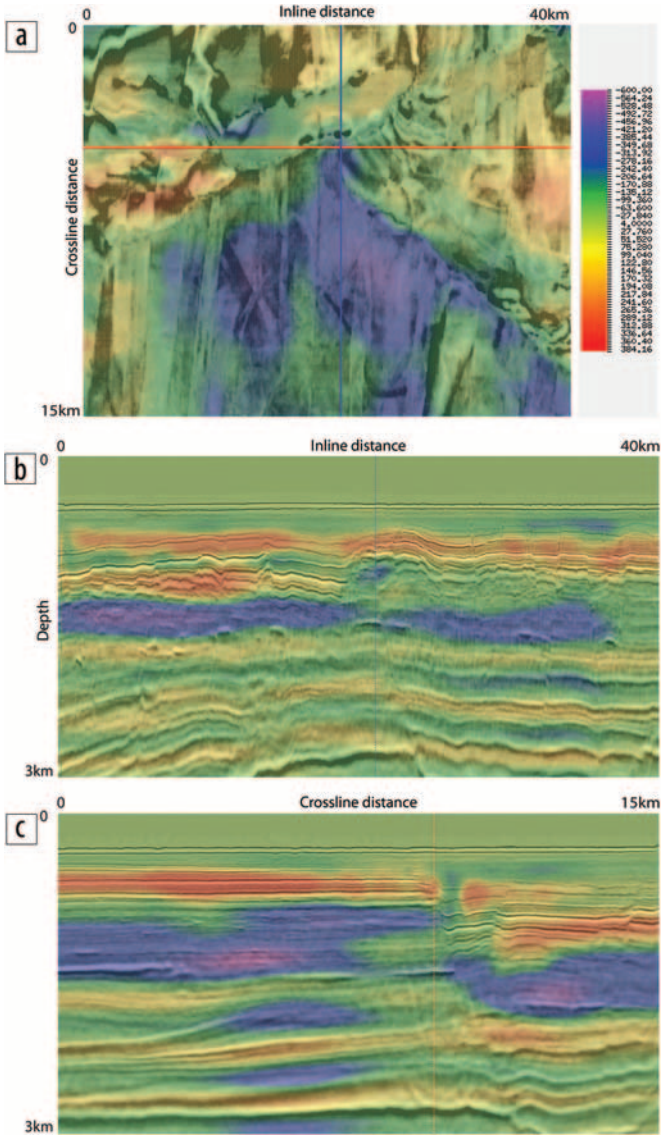

Figure 5. FWI velocity update overlaid on migration stack image. (a) Depth slice at 1050 m. (b) An inline section. (c) A crossline section.

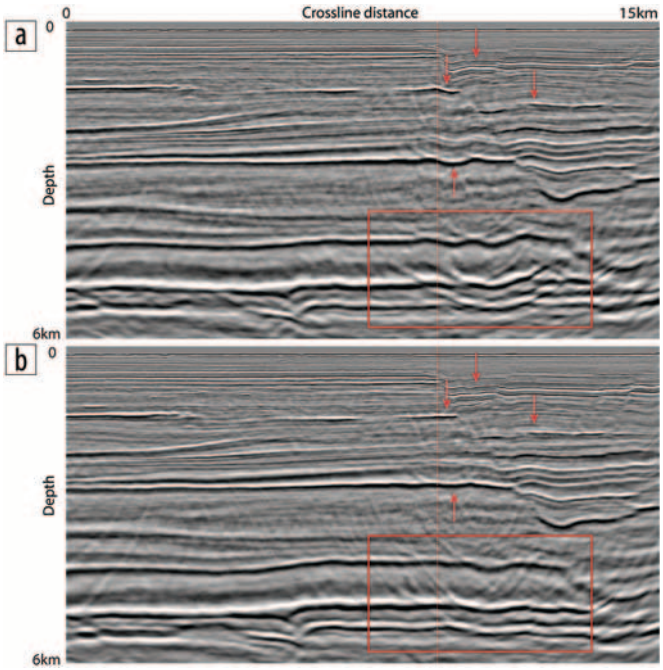

Figure 6. Depth-migration image of a crossline section. (a) Migration with the initial model and (b) migration with the updated model.

bands on top of the FWI velocity generated at the previous inversion stage. This multistage FWI gradually added high-wavenumber structures to the velocity model. Due to the poor illumination of the NAZ acquisition, there are very strong footprint effects observed in the FWI gradients. To avoid killing the details with regular smoothing, image-guided smoothing is proposed to preserve the sharp contrast update, which has been proven much better as it is structural oriented. Because the main contribution of FWI is refraction energy and the main update is in the shallow part (up to 3 km), we run an additional tomography to update the deep portion and also to avoid few overcorrected updates from FWI.

Figure 5a is a depth slice of the FWI velocity update at 1050 m overlaid on the depth Kirchhoff migration image. We can see the sharp contrast from the multistage FWI update. The negative update stops right at the major faults. Figures 5b and Figure 5c are an inline section and a crossline section of FWI update respectively (the locations are marked by the blue line and the red line on Figure 5a), which are also consistent with the real events. The depth-migration image with the initial model is shown in Figure 6a and the image with the updated velocity model is plotted in Figure 6b. From the comparison, we can see the sags are greatly reduced in the fault shadow area (indicated by red arrows), which is more sensible geologically from an interpreter's point of view. The deep events become more continuous and focused (indicated in the red box). We extract the common-image gathers in this crossline section and show them in Figure 7. Not only is the gather flatness improved, but also the broken gathers heal (shown in the red boxes in Figure 7) because of a more accurate model for both the low-wavenumber part and high-wavenumber part.

Conclusions

We present a practical methodology for high-resolution model building with full-waveform inversion for a NAZ data set. We start from a tomographic velocity model and run a multistage FWI. In the first stage, the newly developed dynamic-warping preconditioned FWI is applied to get long-wavelength updates without cycle skipping. Then the conventional L2-norm FWI is utilized to get a higher-resolution update. To reduce the footprint effects caused by NAZ acquisition, we used image-guided smoothing on the FWI gradient, which can preserve the sharp contrast around the faults. A much higher-resolution model update is obtained after FWI. We also run additional tomography after FWI is done. Significant improvements can be seen from both the stacked image and common-image gathers on the Hoop Fault Complex field data example, which proved the effectiveness of our multistage FWI workflow. With this multistage FWI workflow, we believe that we can get more successful examples, not only for NAZ data but also for wide-azimuth acquisition data and ocean-bottom-node (or cable) data. TLE

Acknowledgments

We would like to thank TGS for permission to present this work. We appreciate the helpful discussions from Simon Baldock, Bin Wang, Zhiming Li, Gary Rodriguez, and Jing Chen. We thank Yang He, Rodolfo Hernandez, and Guy Hilburn for tomography guidance. We also thank Connie VanSchuyver for proofreading.

Corresponding author: jian.mao@tgs.com

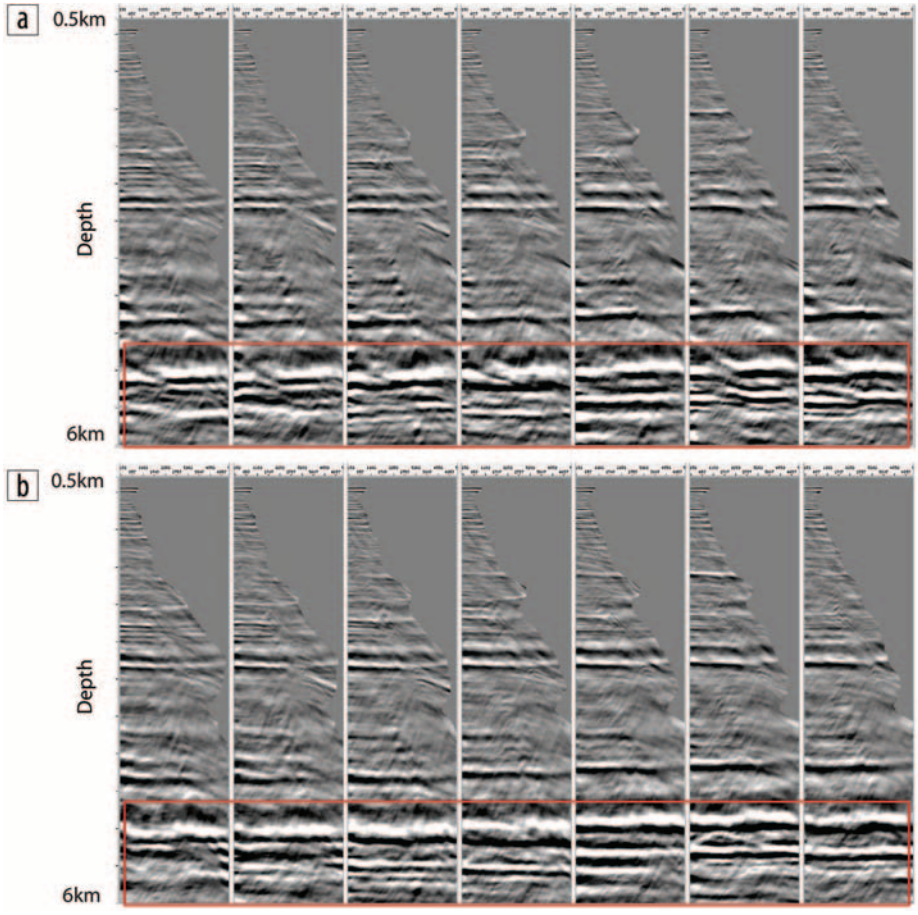

Figure 7. Common-image gathers of a crossline section. (a) CIG with the initial model; (b) CIG with the updated model.

References

Hale, D., 2013, Dynamic warping of seismic images: Geophysics, **78**, no. 2, S105–S115, http://dx.doi.org/10.1190/geo2012-0327.1.

Hart, M., O. Adewumi, C. Lang, G. Hilburn, and G. Rodriguez, 2015, High resolution velocity model building over the Hoop Fault Complex: 85th Annual International Meeting, SEG, Expanded Abstracts, 5189–5193, http://dx.doi.org/10.1190/segam2015-5907902.1.

Hilburn, G., Y. He, Z. Yan, and F. Sherrill, 2014, High-resolution tomographic inversion with image-guided preconditioning and offset-dependent picking: 84th Annual International Meeting, SEG, Expanded Abstracts, 4768–4772, http://dx.doi.org/10.1190/segam2014-1219.1.

Jones, C. E., M. Evans, A. Ratcliffe, G. Conroy, R. Jupp, J. I. Selvage, and L. Ramsey, 2013, Full-waveform inversion in a complex geological setting — A narrow azimuth towed streamer case study from the Barents Sea: 75th EAGE Conference & Exhibition, http://dx.doi.org/10.3997/2214-4609.20130830.

Luo, Y., Y. Ma, Y. Wu, H. Liu, and L. Cao, 2016, Full-traveltime inversion: Geophysics, **81**, no. 5, R261–R274, http://dx.doi.org/10.1190/geo2015-0353.1.

Ma, Y., and D. Hale, 2013, Wave-equation reflection traveltime inversion with dynamic warping and full-waveform inversion: Geophysics, **78**, no. 6, R223–R233, http://dx.doi.org/10.1190/geo2013-0004.1.

Ma, Y., D. Hale, B. Gong, and Z. Meng, 2012, Image-guided sparse-model full waveform inversion: Geophysics, **77**, no. 4, R189–R198, http://dx.doi.org/10.1190/geo2011-0395.1.

Mao, J., R. Wu, and B. Wang, 2012, Multiscale full waveform inversion using GPU: 82nd Annual International Meeting, SEG, Expanded Abstracts, 1–7, http://dx.doi.org/10.1190/segam2012-0575.1.

Pratt, G., C. Shin, and G. J. Hicks, 1998, Gauss-Newton and full Newton methods in frequency-space seismic waveform inversion: Geophysical Journal International, **133**, no. 2, 341–362, http://dx.doi.org/10.1046/j.1365-246X.1998.00498.x.

Rodriguez, G., A. Lundy, M. Hart, C. Lang, J. Cai, I. Chang, and Q. Zhang, 2011, Imaging the Hoop Fault complex via horizon and fault constrained tomography: 81st Annual International meeting, SEG, Expanded Abstracts, 4025–4029, http://dx.doi.org/10.1190/1.3628047.

Sheng, J., A. Leeds, M. Buddensiek, and G. T. Schuster, 2006, Early arrival waveform tomography on near-surface refraction data: Geophysics, **71**, no. 4, U47–U57, http://dx.doi.org/10.1190/1.2210969.

Shin, C., and Y. H. Cha, 2009, Waveform inversion in the Laplace-Fourier domain: Geophysical Journal International, **177**, no. 3, 1067–1079, http://dx.doi.org/10.1111/j.1365-246X.2009.04102.x.

Tarantola, A., 1984, Inversion of seismic reflection data in the acoustic approximation: Geophysics, **49**, no. 8, 1259–1266, http://dx.doi.org/10.1190/1.1441754.

Virieux, J., and S. Operto, 2009, An overview of full waveform inversion in exploration geophysics: Geophysics, **74**, no. 6, WCC1–WCC26, http://dx.doi.org/10.1190/1.3238367.

Warner, M., A. Ratcliffe, T. Nangoo, J. Morgan, A. Umpleby, N. Shah, V. Vinje, I. Štekl, L. Guasch, C. Win, G. Conroy, and A. Bertrand, 2013, Anisotropic 3D full-waveform inversion: Geophysics, **78**, no. 2, R59–R80, http://dx.doi.org/10.1190/geo2012-0338.1.

Warner, M., and L. Guasch, 2015, Robust adaptive waveform inversion: 85th Annual International meeting, SEG, Expanded Abstracts, 1059–1063, http://dx.doi.org/10.1190/segam2015-5853026.1.

Wu, R., J. Luo, and B. Wu, 2014, Seismic envelope inversion and modulation signal model: Geophysics, **79**, no. 3, WA13–WA24, http://dx.doi.org/10.1190/geo2013-0294.1.